Engineering Failure Analysis 170 (2025) 109273

Contents lists available at ScienceDirect

Engineering Failure Analysis

journal homepage: www.elsevier.com/locate/engfailanal

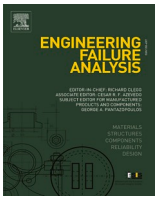

Atmospheric corrosion of welded dissimilar T-joints made of steel and improvements in the corrosion prediction model

Shuang Sun [a,1], Chenying Liu [a,1,*], Gonçalo Ferraz [b], Burak Karabulut [b], Brent Verhoeven [b], Xiongfeng Ruan [b,a], Raf Dewil [b,a], Barbara Rossi [a,b]

[a] Department of Engineering Science, University of Oxford, Oxford, United Kingdom
[b] Faculty of Engineering Technology, KU Leuven, Sint-Katelijne-Waver, Belgium

ARTICLE INFO

Keywords:
Atmospheric corrosion
Dissimilar weld
Duplex stainless steel
High-strength carbon steel
Corrosion database
Corrosion prediction

ABSTRACT

This paper investigates the corrosion behaviour of dissimilar T-joints made of duplex stainless steel and carbon steel under atmospheric environments. Stainless steel grade EN1.4062 was welded to two different carbon steel grades, S355J2 and P460NL2, via gas metal arc welding to form T-joints. The fabricated specimens were subjected to 12-month exposure tests in four mildly corrosive environments distributed across 3 different European countries: Belgium, England, and Portugal. Uniform, galvanic, and pitting corrosion was observed and analysed in detail. In particular, the CS plates, nearby HAZs, and junctions between the SS and CS plates are areas with relatively low corrosion resistance. This finding provides guidance for the use of protective coating systems for dissimilar weldments. The evaluation of corrosion rates obtained in this study and from previous literature suggests that some prediction models are too conservative for atmospheric corrosion under mildly corrosive environments. Two mathematical functions for corrosion rate prediction have thus been recalibrated from a newly formulated corrosion database. A model with the best accuracy for carbon steel under similar conditions is finally identified.

1. Introduction

Stainless steel (SS) and coated carbon steel (CS) are used in modern structures because of their high strength and durability, which leads to cost effectiveness. Their indefinitely recyclable nature also offers a circular solution to the construction industry. Depending on their chemical compositions, the two metals greatly differ in cost, strength, ductility, and corrosion resistance. SS contains a high proportion of chromium (> 10.5 % in mass), which reacts with oxygen to form a self-repairing protective layer that prevents corrosion. CS is susceptible to corrosion and therefore requires a protective coating but generally has a relatively high supply availability at a rather low price.

Recent studies have revealed that hybrid solutions, i.e., those that combine both types of metals, can provide benefits such as tailored corrosion performance, improved sustainability, and reduced lifespan cost [1,2,3,4,5]. A case study by Karabulut et al. revealed that partially replacing carbon steel in a girder bridge with duplex stainless steel can lower both material use and maintenance costs [2]. Hence, there has been a surge of interest in exploring hybrid SS-CS structures in built environments to reduce the overall cost

* Corresponding author.
E-mail addresses: chenying.liu@chch.ox.ac.uk, chenying.liu@eng.ox.ac.uk (C. Liu).
[1] The first two authors contributed equally to this work.

https://doi.org/10.1016/j.engfailanal.2025.109273
Received 12 October 2024; Received in revised form 4 December 2024; Accepted 4 January 2025
Available online 6 January 2025

and increase corrosion resistance.

SS and CS alloys can be connected via dissimilar welding. This process causes microstructural changes in the weld nugget and heat affected zone (HAZ) [6,7,8]. In particular, the corrosion resistance of dissimilar weldments may worsen considerably. Recent scientific studies (see Table 1, [6,7,8,9,10,11,12]) have improved the understanding of the corrosion behavior of SS-CS dissimilar welds and provided guidance for effectively mitigating these risks.

In the literature, corrosion of all families of SS has been investigated, i.e., ferritic, austenitic, and duplex, whereas low-carbon steel has been the primary focus of CS plates. SS has a wide range of yield strengths from 205 to 560 MPa, whereas the yield strength of previously examined CS is only up to 350 MPa. Different welding processes have been employed using common fillers such as E2209. Standard electrochemical corrosion tests are usually preferred. Important conclusions include that greater corrosion of the weldment is due to galvanic corrosion (see [12]) and that significantly higher corrosion resistance is due to appropriate welding methods and fillers (see [6,7,8,9,10,11]).

Little information exists on the corrosion behaviour of dissimilar welds outside of laboratory conditions. Additionally, while a few duplex SS samples with yield strengths of up to 560 MPa have been studied, there is usually a mismatch in the yield strengths of the associated CS plates. All these factors have made it rather difficult to assess the true potential of dissimilar SS-CS welds for construction under real conditions.

To address this research gap, this study focuses on the atmospheric corrosion of SS-CS dissimilar welds in four European locations. Specifically, we selected stainless duplex steel (i.e., EN1.4062) and low-carbon steel (i.e., S355J2 and P460NL2) as base materials to align with industrial practice and select grades with similar mechanical performance. Following the standard gas metal arc welding process to form T-type joints between the two types of steel, a total of 84 samples were designed and fabricated according to European standards ISO 8501–1 [13]. They were subsequently placed in four European geographical locations for a year-long monitored atmospheric corrosion test. The morphology, chemical composition, and corrosion rate of each sample were analyzed, with a focus on the heat-affected zone (HAZ) and junction between two plates. Based on these findings, guidance is provided on the necessary protective coating on SS-CS welds. Finally, prediction models for CS corrosion are evaluated, and a corrosion database is formulated for carbon steel under mildly corrosive environments to recalibrate those models. The results support the standard set in ISO 9223:2012 [14], i.e., corrosion of metals and alloys.

2. Experimental procedure

2.1. Base metals and specimen preparation

The lean duplex grade, i.e., EN1.4062, is chosen as the SS base material because of its high yield strength compared with austenitic grades, cost effectiveness compared with traditional duplex grades, and good corrosion resistance in medium corrosive environments. Two types of CS grades are considered in this study: the European Standard structural steel S355J2 and the high-quality pressure vessel steel P460NL2. Both grades are low-carbon, readily weldable, and increasingly employed in bridge structures. The strength and chemical composition of each material are given in Table 2, according to EN 10025–2 [15] and EN 10025–3 [16 17,4,18].

Table 1
Recent studies of dissimilar welds between SS and CS.

Refs.	SS	Strength[1] [MPa]	CS	Strength [MPa]	Thickness[2] [mm]	Welding	Filler	Corrosion Test
[12]	N/A (F[3])	300 – 400	N/A	N/A	20	Laser	N/A	EC[12]
[7]	AISI 304 (A[4])	205	AISI 1020 (LC[6])	350	15	GTAW[8]	N/A	EC
[7]	AISI 304 (A)	205	AISI 1020 (LC)	350	15	SMAW[9]	N/A	EC
[9]	AISI 304 (A)	205	Unspecified (LC)	N/A	6	GTAW	ER309L	3.5 wt% NaCl
[10]	S30408 (A)	310	12Cr2Mo1R (LC)	310	40	GTAW[10]	N/A	3.5 wt% NaCl
[11]	UNS 31803 (D[5])	480	IS 2062 (LC)	250	5	SMAW	E2209, E309	1 M NaCl, 1 M H_2SO_4
[8]	ER 2209 (D)	560	ASTM A516-60 (LC)	220	12	GMAW[11]	ER2209	EC
[6]	2205 (D)	448	16MnR (LA[7])	345	8	GTAW	E(R)2209	3.5 wt% NaCl

[1] Strength: 0.2% proof strength (yield strength).
[2] Thickness: base materials come with a plate shape and are then welded together.
[3] F: ferritic.
[4] A: austenitic.
[5] D: duplex.
[6] LC: low carbon, also known as mild steel or plain C.
[7] LA: low alloy.
[8] GTAW: gas tungsten arc welding.
[9] SMAW: shield metal arc welding.
[10] combined with submerged arc welding.
[11] GMAW: gas metal arc welding.
[12] EC: electrochemical corrosion with unspecified information given on the solution.

The base materials are joined by GMAW using a 309LSi electrode with a diameter of 1 mm. The welding process follows the standards set in BS EN 1011 [17]. The specific welding parameters are based on the optimal selection given by Cools and Staepels [4] and given in Table 3. Long samples were welded and then cut into small specimens for exposure. Abrasive blast cleaning was conducted to remove weld notches and match the usual requirements for steel plates prescribed in steel bridge specifications [18], i.e., $Sa2^{1/2}$ surface quality.

2.2. Sample racks

As shown in Fig. 1, seven types of configurations are investigated. The first three columns (a − c) are three base steels without welding and were used as control groups. The plate sizes and thicknesses are annotated on the left side. The middle two columns (d − e) are T-joints of SS and CS with weldments, whose geometric parameters are given on the right side. The last two columns (f − g) depict parts of the welded T-joints where the CS part has been removed to exclude their influence during the atmospheric exposure program. Two holes were drilled in each specimen to be attached to a test frame with rip-ties. The data collection equipment is also illustrated (see more details in subsection 2.3.2). As shown in Fig. 1, three rows of the same configurations were made for repeatability [19]. The test specimens were directly exposed away from any shelter. The height of the lowest row of samples was 75 cm above ground level to prevent rain splashes. The specimens were inclined at an angle of 45° facing south for maximum sunlight exposure.

2.3. Atmospheric exposure preparation

2.3.1. Test sites

Four European cities were chosen for the exposure experiments. The environmental corrosivity of each city is closely related to its distance to the sea and to the road with deicing salts. Specifically, the four cities, i.e., Sint-Katelijne-Waver (Belgium), Oxford (United Kingdom), Casalinho da Foz (Portugal), and Knokke-Heist (Belgium), have the following distances to the sea: 40.9 km, 96.5 km, 18.8 km, and 0.8 km. All test sites were located near the meteorological stations of each city, with distances to the road with deicing salts ranging from 0.01–0.1 km. According to EN1993 Eurocode 3 [20], the corrosivity of each geographical location is *low* except for that of Knokke-Heist, which is *medium*.

2.3.2. Experimental measurements

The exposure program started in September 2021, and the specimens were withdrawn after 12 months in August 2022. The environmental parameters influencing the corrosion of steels, i.e., chloride content, temperature, and humidity, were monitored continuously at each test site. Specifically, the chloride deposit was collected using a piece of dry gauze that was stretched and held in a Plexiglas frame using the “dry plate” technique [21], as shown in Fig. 1 (bottom left). The gauze was washed each month, and the amount of deposited chloride was evaluated using ion chromatography. The gauze was sheltered to provide maximum protection from rain. The temperature and relative humidity were recorded using a UX100-003 data logger, as shown in Fig. 1 (bottom right). The equipment was placed inside an insulation box where the air flow was allowed from the sides and bottom. The influence of radiation reflection from the metal surface below was minimised.

2.4. Post-corrosion assessment

2.4.1. Experimental methodology

After one year of exposure, the samples were first subjected to microscopic examination using a Hirox KH-8700 digital microscope. Qualitative analysis was conducted by scanning electron microscopy (SEM) and energy dispersive spectroscopy (EDS).

Afterwards, the corrosion rate of each sample was evaluated based on its overall mass loss. The loose corrosion products on each specimen were removed according to ASTM G1-03 [22], i.e., the corroded specimens were chemically cleaned in 1000 mL of solution with 100 mL of nitric acid and 20 mL of hydrofluoric acid at 25 °C for 10 min. The cleaning procedure was repeated six times until weight loss stagnated. After each cycle, the specimens were subsequently measured on a digital scale with an accuracy of ± 0.001 g to calculate the difference from their original weights.

2.4.2. Considered theoretical models for comparison

The collected corrosion data are compared with theoretical predictions using dose–response functions based on previous literature and industrial standards, the details of which are summarised in Table 4. The environmental parameters measured or collected from

Table 2
Minimum yield strength and chemical composition of the selected steels in this study.

Grade	Strength [MPa]	Chemical composition [wt.%]							
		C	*Si*	*Mn*	*Cr*	*Ni*	*Mo*	*Cu*	*N*
EN1.4062	530	0.02	–	2.00	22.00	2.00	0.40	–	0.20
S355J2	355	0.20	0.34	1.46	0.05	0.03	0.01	0.04	–
P460NL2	460	0.20	0.32	1.10	0.02	–	0.01	0.04	–
309LSi	410	0.02	0.80	1.80	23.50	13.50	–	–	–

Table 3
Welding parameters used to fabricate dissimilar T-joints.

Horizontal plate	Vertical plate	Welding material	Gas	Welding parameters			
				U [V]	*I* [A]	*V* [cm/min]	*Q* [kJ/mm]
EN1.4062	S355J2/P460NL2	309LSi	Arcal 129	27	253	45.2	0.73

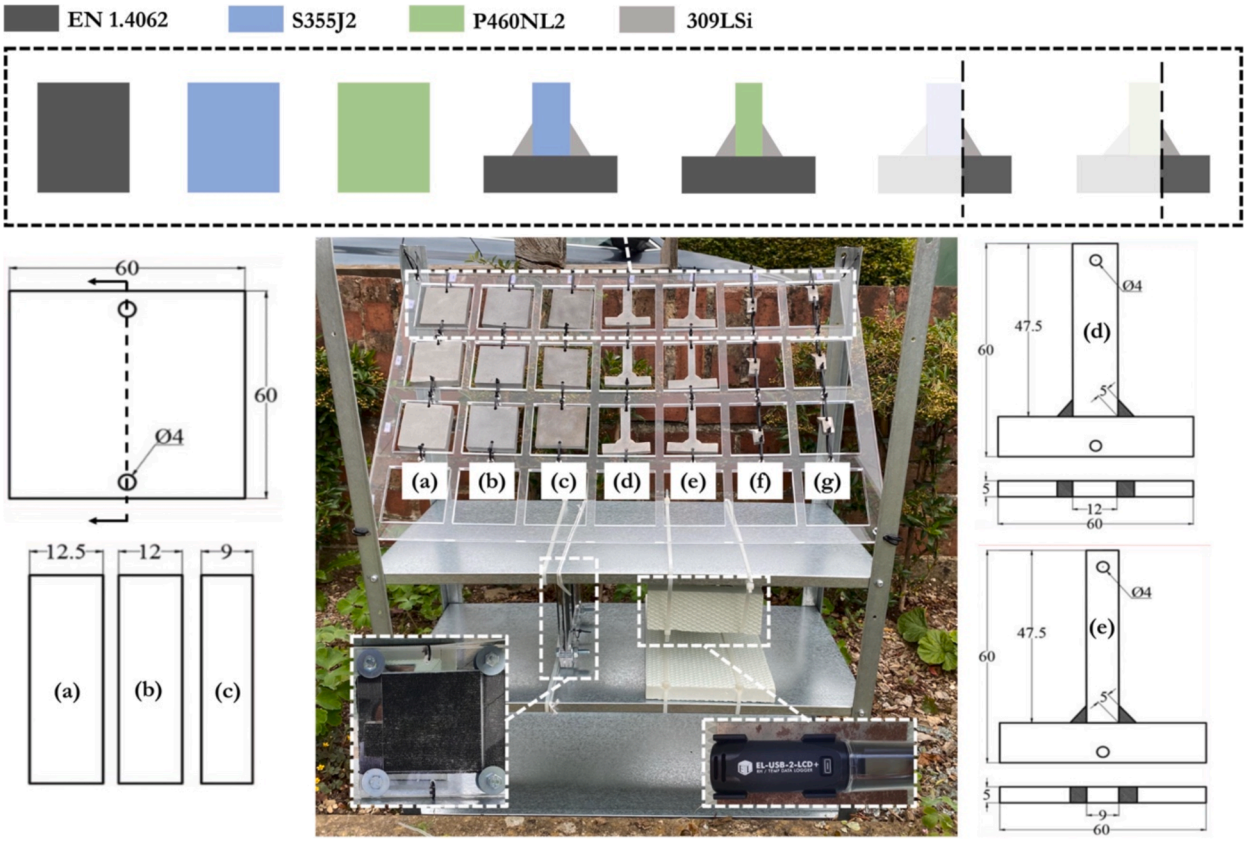

Fig. 1. Experiment test sample racks with (a) EN1.4062 base plate; (b) S355J2 base plate; (c) P460NL2 base plate; (d) dissimilar T-joint of EN1.4062/S355J2 with 309LSi electrode; (e) dissimilar T-joint of EN1.4062/P460NL2 with 309LSi electrode; (f) dissimilar weld of EN1.4062/309LSi (S355J2 removed); (g) dissimilar weld of EN1.4062/309LSi (P460NL2 removed).

local stations are taken as the inputs of these functions. These parameters are applied to predict the first-year corrosion rate of carbon steel, R_{corr}, which is expressed in units of μm/a. Additionally, it should be noted that f(T) below represents a correction factor specifically for steel.

3. Results and discussion

3.1. Environmental parameters

The annual averages of relative humidity, temperature, time of wetness, sulphur dioxide deposition rate, and chloride deposition rate at all test sites for the period spanning September 2021 to August 2022 are summarised in Table 5. The data are obtained from experimental measurements as well as the European Environment Agency [27] and meteorological stations.

More detailed monthly data are given in Fig. 2. The temperature exhibited a roughly unimodal distribution throughout the year. The deposition rates of sulphur dioxide at all test sites are below 4 mg/(m^2·d), indicating the lowest level of pollution according to ISO 9223 [14]. All the test sites have a medium chloride deposition rate, whereas the coastal city, Knokke-Heist, has the highest annual average. The humidity level was relatively consistent throughout the year, and the time of wetness observed ranged from 3349 h/a to 5030 h/a. This duration indicates the long presence of water films, which are likely to act as electrolytes and accelerate the atmospheric corrosion of steels.

Table 4
Dose-response functions for CS corrosion published in the literature.

Function	N[1]	Variable	Ref.(year)
Lien & San $R_{corr} = 0.0157 \times RH^{2.3} \times \left(\frac{\tau}{3800}\right)^{0.15} \times \left(1+\frac{P_d}{50}\right)^{0.22} \times e^{-0.0019\times(T+20)}$	21	RH[2], T[3], τ[4], P_d[5]	[23] (2002)
Knotkova et al. $R_{corr} = 0.091 \times P_d^{0.56} \times \tau^{0.52} \times e^{f(T)} + 0.158 \times S_d^{0.58} \times \tau^{0.25} \times e^{0.05\times T}$ $f(T) = 0.103 \times (T-10) \quad T \le 10^{\circ}C$ $f(T) = -0.059 \times (T-10) \quad T > 10^{\circ}C$	125	T, P_d, S_d[6], τ	[24] (2003)
Klinesmith et al. $R_{corr} = 13.4 \times \left(\frac{\tau}{3800}\right)^{0.46} \times \left(1+\frac{P_d}{25}\right)^{0.62} \times \left(1+\frac{S_d}{50}\right)^{0.34} \times e^{0.02\times(T+20)}$	190	T, P_d, S_d, τ	[25] (2007)
Knotkova et al. $R_{corr} = 0.09 \times S_d^{0.56} \times \tau^{0.53} \times e^{f(T)} + 0.24 \times P_d^{0.47} \times \tau^{0.25} \times e^{0.05\times T}$ $f(T) = 0.098 \times (T-10) \quad T \le 10^{\circ}C$ $f(T) = -0.087 \times (T-10) \quad T > 10^{\circ}C$	119	T, P_d, S_d, τ	[26] (2010)
Standard ISO 9223 $R_{corr} = 1.77 \times P_d^{0.52} \times e^{0.02\times RH+f(T)} + 0.108 \times S_d^{0.62} \times e^{0.033\times RH+0.04\times T}$ $f(T) = 0.150 \times (T-10) \quad T \le 10^{\circ}C$ $f(T) = -0.054 \times (T-10) \quad T > 10^{\circ}C$	128	RH, T, P_d, S_d	[14] (2012)

[1] N: Number of data points.
[2] RH: the annual average relative humidity [%].
[3] T: the annual average temperature [°C].
[4] τ: the annual average time of wetness [h/a], i.e., the duration during which the relative humidity exceeds 80 % and the temperature remains above 0 °C.
[5] P_d: the annual average sulphur dioxide deposition rate [mg/(m^2·d)].
[6] S_d: the annual average chloride deposition rate [mg/(m^2·d)].

Table 5
Annual average environmental parameters at the four sites from Sep. 2021 to Aug. 2022.

Site	RH[%]	T [°C]	P_d [mg/(m^2·d)]	S_d [mg/(m^2·d)]	Rainfall [mm]	τ [h/a]
Source	M[1]	M	S[2]	M	S	C[3]
SKW	73.0	13.2	1.2	8.0	292	3721
Oxford	79.2	12.2	2.5	7.6	302	4991
Casalinho da Foz	79.8	15.8	0.7	6.4	280	5030
Knokke-Heist	75.5	13.0	1.2	17.0	163	3349

[1] M: monitored.
[2] S: station.
[3] C: calculated.

3.2. Microstructure morphology of the corroded samples

3.2.1. Uniform corrosion and morphology of the rust layer

Pictures of the corroded T-joints after the year-long exposure program are shown in Fig. 3. The rust formation of each specimen mainly appeared in the CS plates, with little or even no corrosion observed on the duplex SS surface or its nearby edges with the T-joints.

For the CS plates, the exact rust morphology varies by geographical site and steel grade. As shown in Fig. 3, specimens from the first three sites exhibit yellow rust (an indication of α-$FeOOH$ and Fe_3O_4), whereas those at Knokke-Heist exhibit grey-green rust (an indication of γ-$FeOOH$). The colour difference can be attributed to the effect of rain washing. For a CS plate, there are normally two layers of rust on its surface. The inner layer is fine and compact [28], and the outer layer has a loose and more porous structure [28,29]. The outer one is less stable and can easily flake off during rain. During the exposure program, the rainfall at Knokke-Heist was significantly less than that at the other locations; hence, the outer surface was mostly maintained.

To compare the corrosion behaviors between different CS grades, the specimens at Knokke-Heist are taken as an example. Enlarged microscopic images are obtained for both grades. As shown in Fig. 4, the rust layer on steel S355J2 was thinner, indicating better corrosion resistance. This phenomenon is likely due to the difference in chemical composition between the two CS grades. According to Table 2, S355J2 has a relatively high proportion of nickel and chromium, which has been found to facilitate the formation of a protective layer [28,29,30,31,32,33]. Hence, only relatively loose rusts exist on the S355J2 grade, while P460NL2 has a wider spread and more uniformly distributed rust layer, which could significantly impact its structural performance.

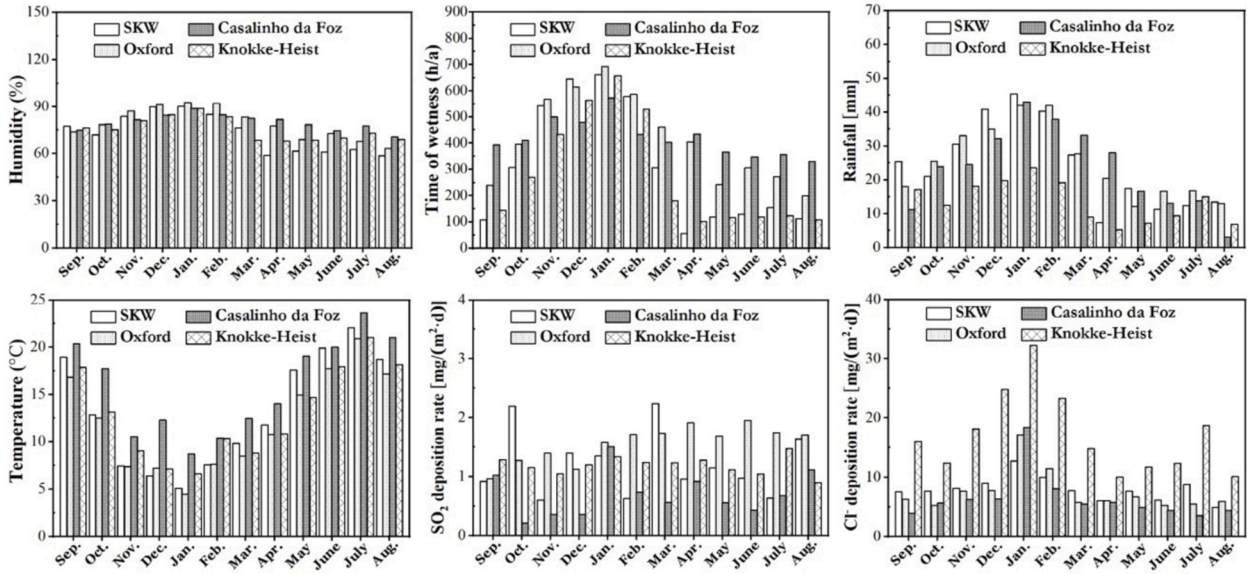

Fig. 2. Monthly average values of humidity, time of wetness, rainfall, temperature, sulphur dioxide deposition rate, and chloride deposition rate from Sep. 2021 to Aug. 2022.

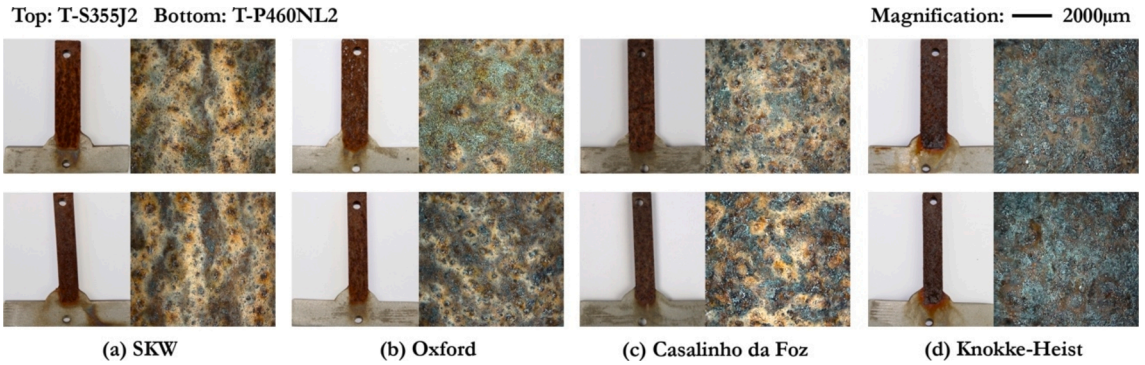

Fig. 3. Corrosion of selected T-joints in the four test sets and the micromorphology of the rust layers.

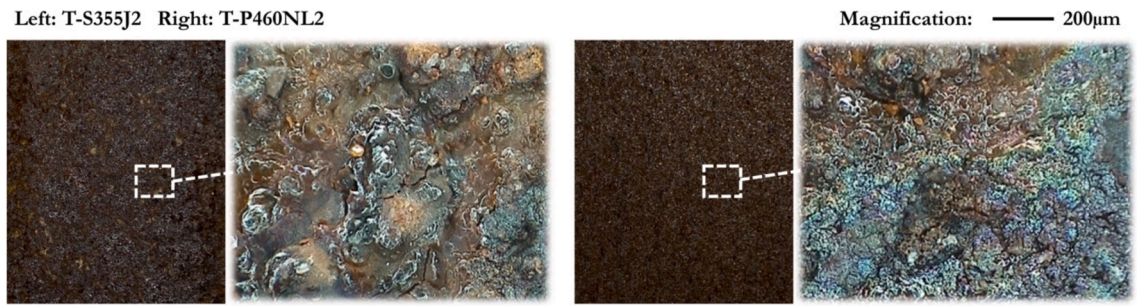

Fig. 4. Morphology of rust layers on carbon steel in Knokke-Heist after year-long exposure.

3.2.2. Galvanic corrosion

While corrosion primarily influences CS plates, galvanic corrosion also occurs; i.e., if two dissimilar metals are connected in a corrosive environment, the less noble metal takes the role of the anode and corrodes at a faster rate than it should [34]. As shown in Fig. 3, the junctions between the CS and SS plates are corroded, whereas those at Knokke-Heist are the most severe, which is attributed to the high chloride deposition rate.

To assess the electrochemical behavior of the studied materials further, grades S355J2 and EN1.4062 were placed in a 1 M sodium

chloride solution for 12 h. The potential of each material was recorded continuously, with EN1.4062 between −0.05 V and −0.1 V and S355J2 between −0.55 V and −0.65 V. Hence, the potential difference between the two grades ranged from + 0.45 V to + 0.6 V. A similar phenomenon was also obtained for grades P460NL2 and EN1.4062. This observation demonstrated potential galvanic corrosion in the experiments and informed the galvanic series of metals in [34].

3.2.3. Pitting corrosion

Pitting corrosion was observed on the CS plates and nearby HAZ after the cleaning procedure. As shown in Fig. 5, the T-joint specimen of grade P460NL2 at Knokke-Heist is taken as an example.

A total of 20 pits were randomly selected across the CS plate and HAZ of each T-joint specimen. The average pit depth is illustrated in Fig. 6(a). In general, more and deeper pits exist on Grade P460NL2 than on Grade S355J2. Additionally, more severe localized corrosion was observed in the HAZ of each sample. The pits found in the HAZ near the CS plate are significantly deeper in Knokke-Heist. This is due to the medium corrosivity at the site where the metal surface almost completely deteriorated due to the high chloride deposition rate. This observation suggests that in such salt-rich environments, a coating system should be implemented as a protection mechanism for dissimilar welds, particularly in the HAZ.

Interestingly, no pits were detected in the HAZ between the austenitic 309LSi filler and the EN1.4062 lean duplex SS plate at any test location. As shown in Fig. 6(b), there is a discernible fusion line between the base metal and filler, which is a result of the difference in the proportion of nickel. Both materials also have similarly high proportions of chromium, which facilitates the formation of protective films against corrosion.

3.3. Atmospheric corrosion rate

3.3.1. Measured corrosion rate by weight loss

Fig. 7(a) depicts the overall mass loss of a certain specimen as a function of the number of cleaning cycles. Two approximately straight lines can be observed. Line AB represents the removal of corrosion products and the steel substrate, whereas line BC depicts the removal of the steel substrate only. Point D represents the mass of the steel substrate at zero cleaning cycles and can be obtained by extrapolating line BC to the ordinate axis. The entire mass loss due to corrosion is the distance between points A and D. According to ASTM G1-03 [22], the corrosion rate is

$$R_{corr} = \frac{KW}{At\rho}$$

where K is the conversion factor 8.76 x 10^7, W is the mass loss [g], A is the exposure area [cm^2], t is the time of exposure [h], and ρ is the density of steel [g/cm^3].

The average corrosion rate of each specimen is summarised in Table 6. According to the corrosivity category defined by ISO 9223 [14], the corrosion level of the SS plates falls into the lowest level C1, and that of all the CS plates falls into C2. As expected, the CS plates corroded at a much faster rate due to the lack of a protective layer, and the S355J2 base plates corroded less than did P460NL2, which aligns with the observed uniform and pitting corrosion behavior. The overall corrosion rates of the T-joints were lower than those of the CS-based plates as a result of the added SS filler and base plates. Compared with those of the samples where the CS plates are entirely removed, i.e., N-S355J2 and N-P460NL2, their corrosion rates are slightly higher than those of the pure SS plates, indicating that dissimilar welds are more susceptible to corrosion.

3.3.2. Corrosion rate by decomposition

To evaluate how much dissimilar welding has influenced the corrosion behavior of the T-joint samples, each specimen is

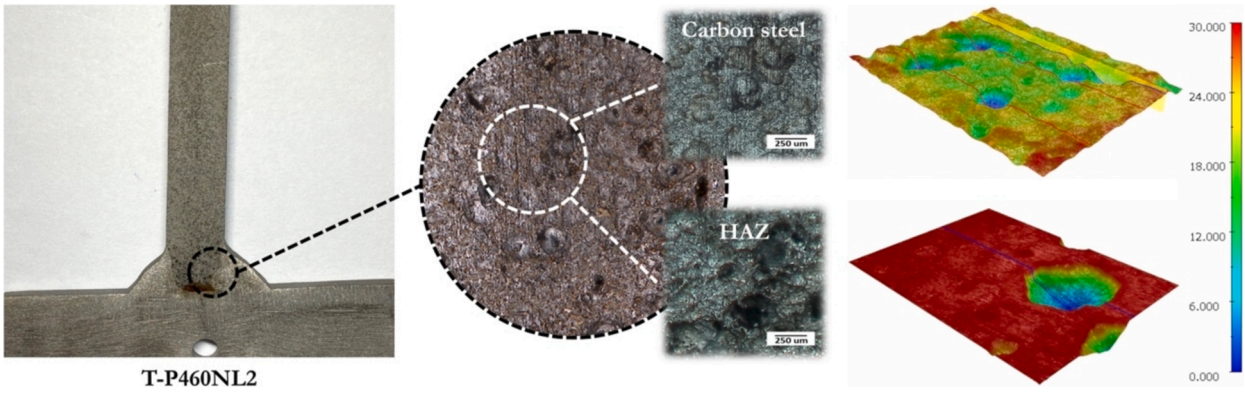

Fig. 5. Pits on carbon steel and HAZ of the T-joint with grade P460NL2 at Knokke-Heist. Color maps showing the pit depths are also indicated where the lowest point is taken as zero.

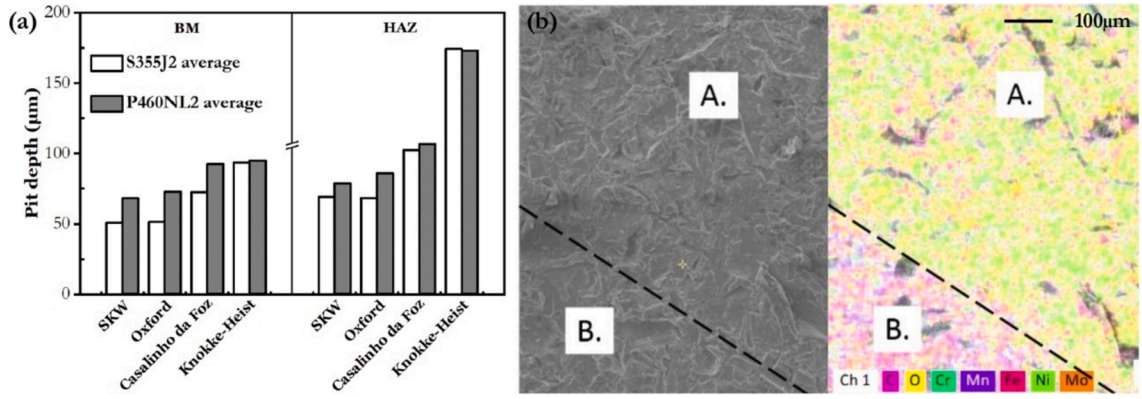

Fig. 6. (a) Average pit depth on the surface of the carbon steel and HAZ. (b) EDS analysis of dissimilar T-joints between EN1.4062 (A) and 309LSi (B) at Knokke-Heist after exposure.

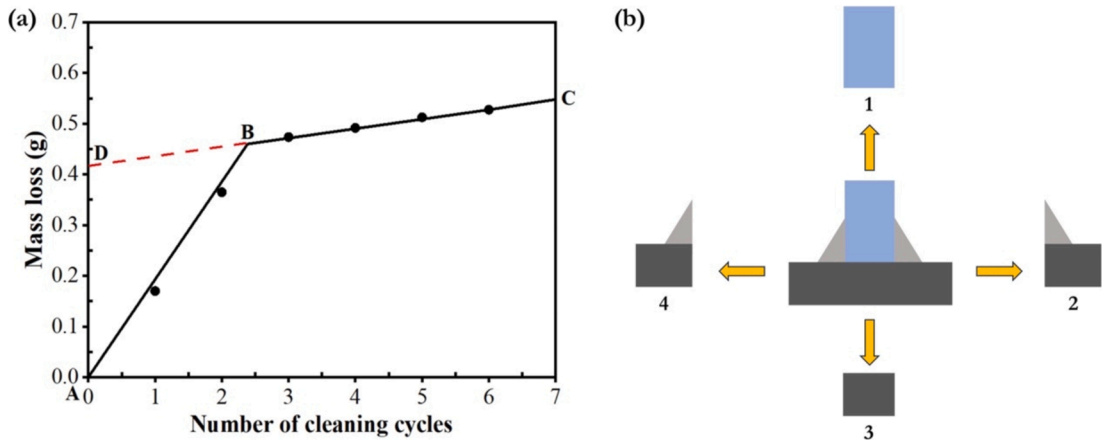

Fig. 7. (a) Stabilised mass loss after chemical cleaning, as exemplified by the result of the T-joint with grade S355J2 in Knokke-Heist. (b) Sectioned T-joint for the decomposed corrosion rate.

Table 6
Averaged corrosion rate measured by weight loss after year-long exposure.

Test site	Corrosion rate [μm/a]						
	EN1.4062	S355J2	P460NL2	T-S355J2	T-P460NL2	N-S355J2	N-P460NL2
SKW	0.42	9.23	12.50	4.63	4.96	1.50	1.59
Oxford	0.47	10.10	13.29	5.74	5.93	1.60	1.68
Casalinho da Foz	0.40	13.12	15.69	6.46	6.89	1.72	1.80
Knokke Heist	0.41	16.02	18.28	8.42	8.87	2.22	2.30

decomposed into four segments, i.e., two base materials and two “carbon-removed joints”, as depicted in Fig. 7(b). The “decomposed” corrosion rate is calculated from the measured rates of individual base metals and carbon-removed joints in Table 6. Hence, the corrosion rate of a T-joint by decomposition becomes

$$DR_{corr} = \frac{\sum_{i=1}^{4} R_{corr-i} A_i}{\sum_{i=1}^{4} A_i}$$

where A_i is the surface area of each section, and the effect of drilled holes has been taken into account for compensation. $R_{corr\text{-}i}$ is the corrosion rate of each segment, as shown in Table 6.

The average decomposed corrosion rates of each T-joint are summarised in Table 7. Compared with the actual rates of the T-joint samples given in Table 6, the decomposed rates are mostly lower except for those of P460NL2 at SKW. The results suggest that, in

general, dissimilar welding accelerates corrosion due to galvanic corrosion between the CS and SS plates and corrosion of the HAZ near the CS plate. The samples at Oxford and Knokke-Heist were subjected to greater impact, as indicated by their relative RoCs.

3.4. Corrosion prediction

3.4.1. Prediction of the carbon steel corrosion rate from the literature

Using the dose–response functions from Table 4 and the environmental parameters in this study, as summarised in Table 5, the corrosion rate of the CS plates can also be estimated at each site. The results are compared in Fig. 8. In general, the models by Knotkova et al. (2003) [24] and Knotkova et al. (2010) [26], as well as those from ISO 9223 standards [14], are relatively closer to the measured results. Moreover, the values predicted from the models by Lien & San (2002) [23] and Klinesmith et al. (2007) [25] exaggerate the potential corrosion behaviors at all sites, which is likely because both functions were originally calibrated for more aggressive marine environments. To improve the prediction accuracy, a corrosion database is formed to calibrate existing dose–response functions in mildly corrosive environments.

3.4.2. Corrosion database

The corrosion data points were collected from prior research where the specimens were subjected to atmospheric conditions similar to those used in this study. Up to 11 literature sources have been identified. Prior to statistical analysis, the manual data filtering process was carried out on the basis of the following criteria: (i) the corrosivity category must be the same as in our study at C_2; (ii) the time of wetness must be maintained below 5500 h/a; (iii) the sulphur dioxide deposition rate and chloride deposition rate must be kept below 4 mg/(m^2·d) and 60 mg/(m^2·d), respectively; and (iv) in cases where meteorological or pollution data are missing, the data point is excluded. After manual filtering, a database consisting of 50 data points is formed in Table 8 from locations worldwide, as marked in Fig. 9.

3.4.3. Calibration of dose–response functions

According to Table 4, when only T, τ, P_d, and S_d are considered, the dose–response functions in the literature [25,26,24,25,26] and [25,26] exhibit two distinct forms. The corrosion rate of each model can be rewritten as

$$R_{corr-a} = a_1 P_d^{a_2} \tau^{a_3} e^{a_4 T + a_5} + a_6 S_d^{a_7} \tau^{a_8} e^{a_9 T}$$

$$R_{corr-b} = b_1 \left(\frac{\tau}{b_2}\right)^{b_3} \left(1 + \frac{P_d}{b_4}\right)^{b_5} \left(1 + \frac{S_d}{b_6}\right)^{b_7} e^{b_8 (T + b_9)}$$

where b_2, b_4, b_6, and b_9 are the average annual wet time, sulphur dioxide deposition rate, chloride deposition rate, and temperature, respectively.

The corrosion database is used to calibrate the unknown coefficients, i.e., a_i and b_i, of the two models, which are determined by the least squares method using the descent algorithm in Python. The final coefficients for the two calibrated dose–response functions, i.e., Model *a* and Model *b*, are given in Table 9.

The 50 corrosion points from the database are plotted in Fig. 10 using models [24,25,26] and [25,26] alongside the calibrated ones to compare the measured and predicted corrosion rates.

The existing three models either overestimate the corrosion rates or have a relatively wide variance. Model *b* has managed to reduce the variance, yet overestimation still exists. In contrast, Model *a* exhibits good alignment between the actual and predicated results with a small variance.

The recalibrated dose functions are finally used to predict the corrosion rates of the CS plates in our study. The results are compared with the measured rates, as shown in Fig. 11. Model *a* has a higher prediction accuracy, which is the same as its similar formats, as shown in Fig. 9. Model *b* has a greater discrepancy, but it should be noted that the difference has already been significantly reduced compared with its equivalence in Fig. 9.

To better compare the efficiency of the two calibrated functions as well as those from the literature, the root mean square error (RMSE) of each model at the four tested sites for two CS grades is calculated as follows, and the results are shown in Table 10.

Table 7
Averaged corrosion rates of T-joints by decomposition after year-long exposure.

Test site	Decomposed T-S355J2		Decomposed T-P460NL2	
	Corrosion rate [μm/a]	RoC[1]	Corrosion rate [μm/a]	RoC
SKW	4.55	−1.73 %	5.21	5.04 %
Oxford	4.97	−13.42 %	5.54	−6.58 %
Casalinho da Foz	6.26	−3.10 %	6.42	−6.82 %
Knokke-Heist	7.69	−8.67 %	7.58	−14.5 %

[1] RoC refers to the ratio of change compared with the actual corrosion rate.

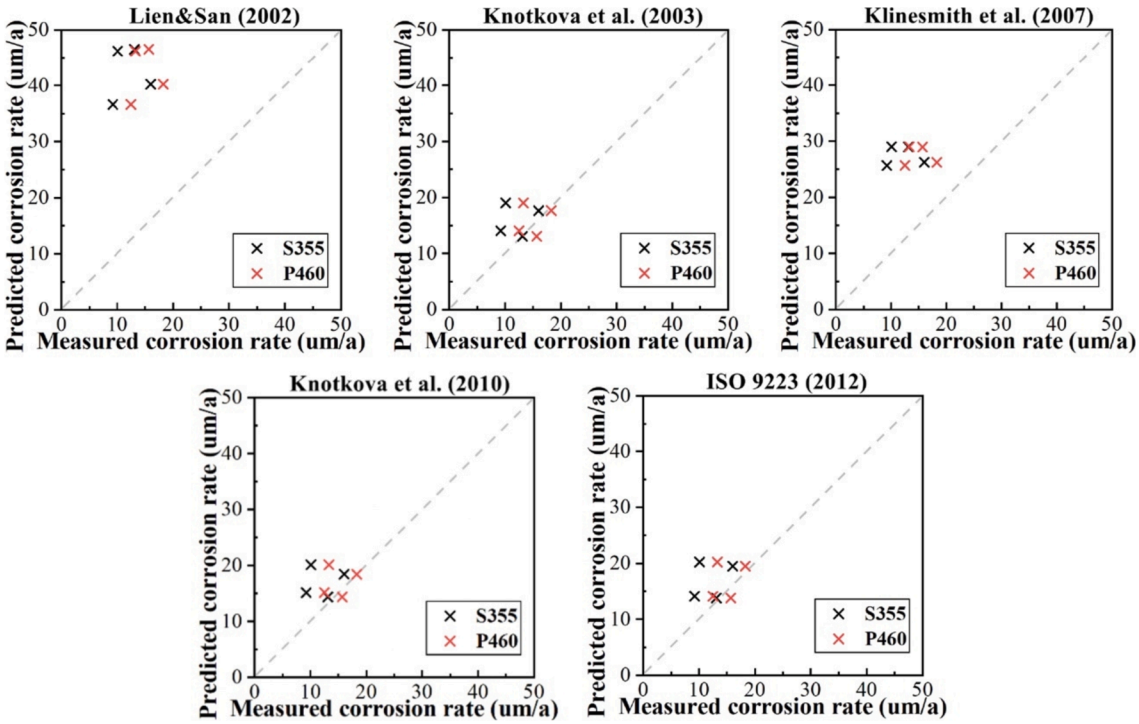

Fig. 8. Comparison between the estimated and measured corrosion rates of carbon.

$$\mathrm{RMSE} = \sqrt{\frac{1}{4}\sum_{i=1}^{4}(f_i - y_i)^2}$$

where f_i is the predicted value and where y_i is the corresponding real-measured value. Among all of them, the new calibrated dose function $R_{corr\text{-}a}$ has the highest prediction accuracy for grade S355J2, whereas the model in [24] outperforms the others for grade P460NL2.

4. Conclusions

This work focuses on the atmospheric corrosion of dissimilar welded T-joints between duplex stainless steel (EN1.4062) and carbon steel (S355J2 and P460NL2) in mildly corrosive environments in European cities. Based on the experimental results and the formulated corrosion database, we have drawn the following conclusions.

Little corrosion was observed on the SS plates and carbon-removed dissimilar welds, whereas uniform corrosion occurred on all the CS plates due to the lack of protection. This suggests that welding did not significantly influence the uniform corrosion of the SS-CS junction. However, galvanic corrosion has significantly influenced the junction between two metals exposed at all geographical locations. This observation was further validated by electrochemical tests and analysis of decomposed corrosion rates. Pitting corrosion also occurred across all the specimens. In particular, the HAZ on the side of the CS exhibited the worst pitting corrosion. This is attributed to decarburisation and grain growth as a result of element diffusion during the welding process. The pits found in the HAZs of the CS grades were notably deeper in the Knokke-Heist samples than in the other samples because of the high chloride deposition rate. In contrast, the HAZ on the side of the SS exhibited high pitting resistance. The EDS results revealed that this phenomenon is due to the high chromium proportion on the SS plate and the weld, which facilitates the formation of protective films against corrosion.

In summary, for a welded dissimilar T-joint made of SS and CS under atmospheric exposure, the CS plate, nearby HAZ, and the junction between the CS and SS plates are the areas most susceptible to corrosion. These findings provide guidance for the implementation of suitable protection in these areas, particularly in salt-rich environments. Moreover, stainless steel plates could be left unprotected to be more cost efficient and environmentally friendly.

Additionally, evaluations of previous studies on corrosion prediction have revealed that some models are inaccurate for atmospheric corrosion. For example, models [24,25,26] and [25,26] lead to higher predicted values than actual corrosion rates do, which will cause unnecessary protection and maintenance. This result is too conservative because these models were formulated in marine environments with high corrosivity. Hence, a new corrosion database was established specifically for mildly corrosive environments, and two prediction functions were subsequently recalibrated from prior research. The comparative analysis revealed the best mode, i.e., corrosion model a, for CS under similar conditions.

Table 8
Database of corrosion tests used in this study compiled from the literature sources.

No.	Location	Grade	T [°C]	τ [h/a]	P_d [mg/(m^2·d)]	S_d [mg/(m^2·d)]	R_{corr} [μm/a]	Refs.
1	Iguazu	AISI 1006	22.9	5387	2.0	1.5	5.8	[26]
2	San Juan	AISI 1006	19.2	911	2.0	1.5	4.6	[26]
3	Ahtari	AISI 1006	4.0	3040	2.8	1.5	9.7	[26]
4	Ahtari	AISI 1006	4.0	3127	2.5	1.5	12.5	[26]
5	Ahtari	AISI 1006	4.1	3381	1.5	1.5	11.3	[26]
6	Birkenes	AISI 1006	5.2	3679	1.4	0.6	21.4	[26]
7	Birkenes	AISI 1006	5.9	4608	1.0	0.6	18.6	[26]
8	Birkenes	AISI 1006	6.3	4187	1.0	0.6	21.8	[26]
9	Birkenes	AISI 1006	7.5	4406	0.8	0.6	17.1	[26]
10	Birkenes	AISI 1006	6.6	3968	0.8	0.6	20.7	[26]
11	Birkenes	AISI 1006	6.2	3679	0.8	0.6	18.6	[26]
12	EI Pardo	AISI 1006	25.3	2427	3.1	1.5	16.3	[35]
13	EI Pardo	AISI 1006	25.3	2716	3.8	1.5	17.0	[35]
14	EI Pardo	AISI 1006	25.2	3522	3.3	1.5	15.6	[35]
15	Los Angeles	CS	17.4	1956	0.5	33.0	17.3	[35]
16	San Juan	CS	18.8	902	2.0	1.5	4.9	[35]
17	Caratinga	CS	21.5	4222	0.8	8.9	8.6	[35]
18	Caratinga	CS	20.9	4222	1.3	7.4	11.5	[35]
19	Caratinga	CS	21.2	4222	1.7	1.6	13.1	[35]
20	Brasilia	CS	20.4	3872	2.0	1.5	12.9	[35]
21	Paulo Afonso	CS	25.9	1507	2.0	1.5	17.3	[35]
22	Cotove	CS	27.0	2891	0.3	1.5	19.6	[35]
23	/	CS	14.4	3504	0.7	20.0	24.5	[36]
24	/	CS	7.5	4406	0.3	2.7	6.2	[36]
25	/	CS	6.6	3968	0.6	29.1	23.5	[36]
26	/	CS	15.3	4845	0.3	2.7	5.4	[36]
27	/	CS	14.2	1500	0.8	3.0	7.4	[36]
28	Chennai	CS	28.3	2791	0.9	1.7	19.0	[37]
29	Delhi	CS	25.5	702	0.2	2.3	13.9	[37]
30	Digha	CS	26.6	2280	1.0	0.8	24.2	[37]
31	Easter Island	SAE 1070	20.5	4690	1.2	50.0	30.0	[38]
32	Mawlamyine	CS	23.8	5532	2.4	1.9	13.9	[39]
33	Yangon	CS	28.9	4002	2.4	3.7	17.3	[39]
34	Mandalay	CS	28.6	1172	2.4	1.2	8.9	[39]
35	Rajiv Gandhi	S235	28.0	1798	1.4	57.3	3.7	[40]
36	Fort George	S235	28.0	1800	1.9	41.6	5.7	[40]
37	Mutual Aid	S235	28.3	1800	1.4	14.5	2.3	[40]
38	Medine Camp de Masque	S235	26.3	3272	1.6	51.4	6.3	[40]
39	Xishuangbanna	Q345	21.5	4320	0.1	0.1	14.9	[41]
40	Phangnga	CS	27.7	5090	2.6	28.6	18.2	[43]
41	Kralupy	CS	11.0	3679	4.0	1.0	5.1	[42]
42	Prague	CS	11.0	3592	4.0	3.0	7.0	[42]
43	Berlin	CS	10.0	4030	1.6	12.0	4.8	[42]
44	Barcelona	CS	15.0	4468	3.0	3.0	6.6	[42]
45	Birkenes	CS	6.0	3942	1.0	7.0	7.3	[42]
46	UEMA	CS	27.2	4920	2.8	8.3	21.8	[44]
47	Santa Rita	CS	27.8	3420	3.0	16.6	24.6	[44]
48	Miranda	CS	28.2	3390	2.0	13.0	24.3	[44]
49	São Mateus	CS	28.2	3897	1.9	9.5	19.8	[44]
50	Peritoró	CS	28.5	3560	1.3	9.5	20.2	[44]

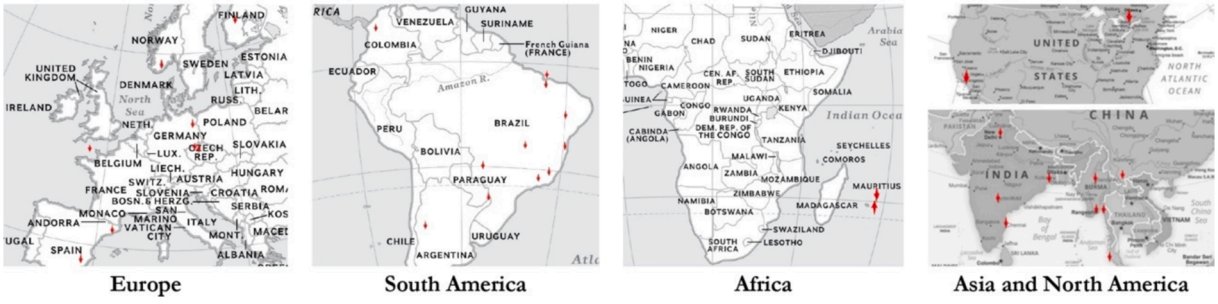

Fig. 9. Maps of the atmospheric corrosion test sites gathered from the literature.

Table 9
The values of all the coefficients are present in the calibrated dose–response functions.

Eq.	a_1	a_2	a_3	a_4	a_5	a_6	a_7	a_8	a_9
$R_{corr\text{-}a}$	7.93	−0.15	0.1	−0.04	0	2.3e-4	−0.12	0.73	0.19
Eq.	b_1	b_2	b_3	b_4	b_5	b_6	b_7	b_8	b_9
$R_{corr\text{-}b}$	16.4	3384	0.3	1.7	0.01	9.4	0.3	0.002	18.7

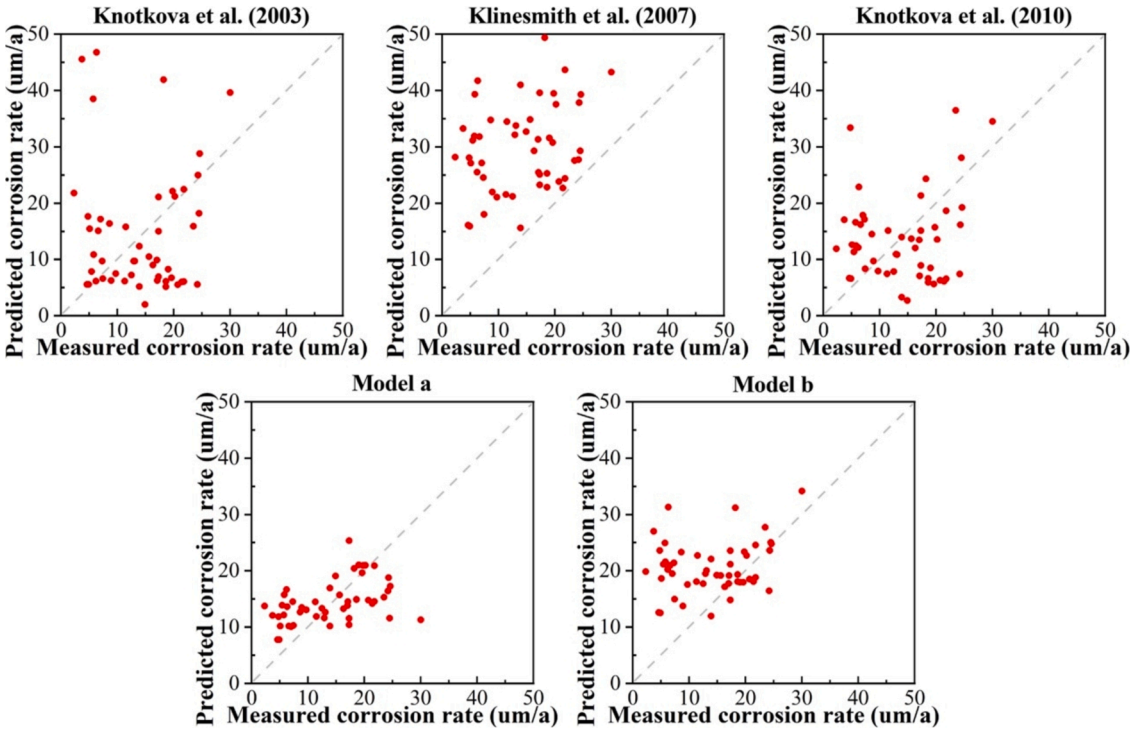

Fig. 10. Predicated corrosion rates from calibrated dose functions versus measured results.

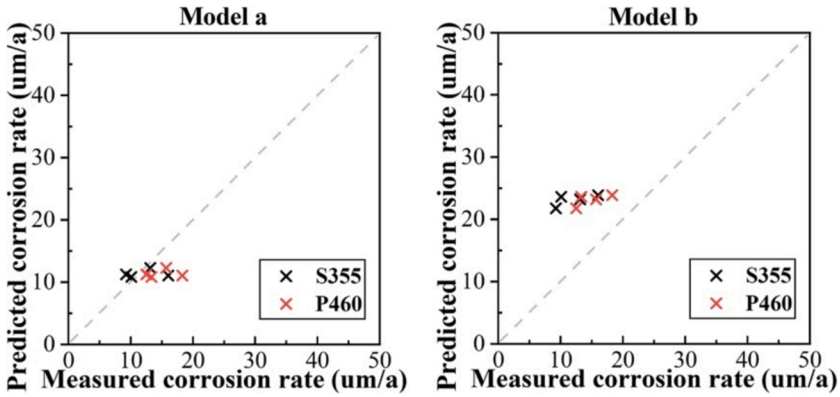

Fig. 11. Predicated corrosion rates from calibrated dose functions versus measured results.

CRediT authorship contribution statement

Shuang Sun: Writing – review & editing, Writing – original draft, Visualization, Validation, Software, Methodology, Investigation, Formal analysis, Data curation. **Chenying Liu:** Writing – review & editing, Writing – original draft, Visualization, Validation, Methodology, Investigation, Formal analysis. **Gonçalo Ferraz:** Writing – review & editing, Methodology, Investigation. **Burak Karabulut:** Writing – review & editing, Investigation, Formal analysis. **Brent Verhoeven:** Writing – review & editing, Investigation.

Table 10
RMSEs of the models from the literature and by calibration of two CS grades. Unit: $g/(m^2 \cdot a)$].

Model	S355J2	P460NL2
Ref. [23]	30.64	27.83
Ref. [24]	5.14	3.26
Ref. [25]	15.69	12.86
Ref. [26]	5.98	3.73
Ref. [14]	5.89	3.73
$R_{corr\text{-}a}$	2.74	4.22
$R_{corr\text{-}b}$	11.22	8.37

Xiongfeng Ruan: Writing – review & editing, Formal analysis. **Raf Dewil:** Writing – review & editing, Resources, Project administration, Funding acquisition. **Barbara Rossi:** Writing – review & editing, Supervision, Resources, Project administration, Methodology, Funding acquisition, Formal analysis, Conceptualization.

Declaration of competing interest

The authors declare that they have no known competing financial interests or personal relationships that could have appeared to influence the work reported in this paper.

Acknowledgements

The authors would like to express their gratitude to ArcelorMittal and Outokumpu for providing the base materials used in this work. Burak Karabulut would also like to gratefully acknowledge the Research Foundadtion Flanders (FWO) for funding his post-doctoral fellowship with the project ID "1256522 N".

Data availability

Data will be made available on request.

References

[1] Y. Bouassida et al., Bridge design to eurocodes Worked examples, vol. 1, no. 1. 2012.
[2] B. Karabulut, G. Ferraz, B. Rossi, Lifecycle cost assessment of high strength carbon and stainless steel girder bridges, J. Environ. Manage. 277 (2021), https://doi.org/10.1016/j.jenvman.2020.111460.
[3] T. Yabuki, Y. Arizumi, T. Shimozato, S. Guezouli, H. Matsusita, and M. Tai, 'Hybrid stainless steel girder for bridge construction', Int. J. Struct. Construct. Eng. vol. 11, no. 5, 2017.
[4] Y.; S. A. Cools, 'Microstructural and mechanical investigations on dissimilar welding', KU Leuven, 2021.
[5] K.; B. N. V. Sterckx, 'Painted, stainless or hybrid steel box girder bridges: Comparative life cycle cost assessment', KU Leuven, 2020.
[6] S. Wang, Q. Ma, and Y. Li, 'Characterization of microstructure, mechanical properties and corrosion resistance of dissimilar welded joint between 2205 duplex stainless steel and 16MnR', Mater. Des. vol. 32, no. 2, 2011, 10.1016/j.matdes.2010.07.012.
[7] W. Chuaiphan, S. Chandra-Ambhorn, S. Niltawach, B. Sornil, Dissimilar welding between AISI 304 stainless steel and AISI 1020 carbon steel plates, Appl. Mech. Mater. (2013), https://doi.org/10.4028/www.scientific.net/AMM.268-270.283.
[8] P. Luchtenberg, P.T. de Campos, P. Soares, C.A.H. Laurindo, O. Maranho, R.D. Torres, Effect of welding energy on the corrosion and tribological properties of duplex stainless steel weld overlay deposited by GMAW/CMT process, Surf. Coat. Technol. 375 (2019), https://doi.org/10.1016/j.surfcoat.2019.07.072.
[9] T.E. Abioye, O.E. Ariwoola, T.I. Ogedengbe, P.K. Farayibi, O.O. Gbadeyan, Effects of welding speed on the microstructure and corrosion behavior of dissimilar gas metal arc weld joints of AISI 304 stainless steel and low carbon steel, Mater. Today Proc. (2019), https://doi.org/10.1016/j.matpr.2019.06.383.
[10] Y. Huang, et al., Microstructure and corrosion characterization of weld metal in stainless steel and low carbon steel joint under different heat input, Mater. Today Commun. 29 (2021), https://doi.org/10.1016/j.mtcomm.2021.102948.
[11] P. B. Srinivasan, V. Muthupandi, W. Dietzel, and V. Sivan, 'An assessment of impact strength and corrosion behaviour of shielded metal arc welded dissimilar weldments between UNS 31803 and IS 2062 steels', Mater. Des. vol. 27, no. 3, 2006, 10.1016/j.matdes.2004.10.019.
[12] W. Wu, S. Hu, J. Shen, Microstructure, mechanical properties and corrosion behavior of laser welded dissimilar joints between ferritic stainless steel and carbon steel, Mater. Des. 65 (2015), https://doi.org/10.1016/j.matdes.2014.09.064.
[13] ISO 8501-1:2007 Preparation of steel substrates before application of paints and related products — Visual assessment of surface cleanliness Part 1: Rust grades and preparation grades of uncoated steel substrates and of steel substrates after overall removal of previous coatings. 2007.
[14] ISO, 'Corrosion of metals and alloys – Corrosivity of atmospheres – Classification, determination and estimation', ISO FDIS, vol. 13B, 2012.
[15] (CEN) European Committee for Standardisation, 'BS EN 10025-2:2004 Hot rolled products of structural steels. Part 2: Technical delivery conditions for non-alloy structural steels', British Standard, vol. 2, 2004.
[16] British Standards, 'Hot rolled products of structural steels— Part 3: Technical delivery conditions for normalized/normalized rolled weldable fine grain structural steels', BS EN 10025-3:2004, vol. 3, 2004.
[17] BS 1011-1-2009, 'BS 1011-1-2009 Welding—Recommendations for welding of metallic materials—Part 1: General guidance for arc welding', Bs En 1011-4: 2000, vol. 3, no. 1, 2000.
[18] Y. Fujino, 'Corrosion protection of steel bridges', Corrosion Engineering, vol. 38, no. 10, 1989, 10.3323/jcorr1974.38.10_546.
[19] ISO 8565, 'Metals and Alloys. Atmospheric Corrosion Testing. General Requirements', 2011.
[20] J. C. Taylor, ' EN1993 Eurocode 3: Design of steel structures ', Proceedings of the Institution of Civil Engineers - Civil Engineering, vol. 144, no. 6, 2001, 10.1680/cien.2001.144.6.29.
[21] International Organization for Standardization, 'Corrosion of metals and alloys-Corrosivity of atmospheres-Measurement of environmental parameters affecting corrosivity of atmospheres Corrosion', Reference number ISO, vol. 9225, 2012.

[22] A. G1-03, 'Standard Practice for Preparing, Cleaning, and Evaluating Corrosion Test Specimens.', ASTM Special Technical Publication, no. Reapproved, 2017.
[23] L.T.H. Lien, P.T. San, The effect of environmental factors in carbon steel atmospheric corrosion; The prediction of corrosion, ASTM Spec. Tech. Publ. (2002), https://doi.org/10.1520/stp10886s.
[24] V. Kucera et al., 'UN/ECE ICP materials dose-response functions for the multi-pollutant situation', Water, Air, Soil Pollution: Focus, vol. 7, no. 1–3, 2007, 10.1007/s11267-006-9080-z.
[25] D. E. Klinesmith, R. H. McCuen, and P. Albrecht, 'Effect of environmental conditions on corrosion rates', J. Mater. Civil Eng. vol. 19, no. 2, 2007, 10.1061/(asce)0899-1561(2007)19:2(121).
[26] D. Knotkova, K. Kreislova, and S. W. Dean, ISOCORRAG international atmospheric exposure program: summary of results. 2010. 10.1520/ds71-eb.
[27] 'European Environment Agency', 2024. Accessed: Jul. 24, 2024. [Online]. Available: https://www.eea.europa.eu/en.
[28] X. L. Gao, Y. Han, G. Q. Fu, M. Y. Zhu, and X. Z. Zhang, 'Evolution of the rust layers formed on carbon and weathering steels in environment containing chloride ions', Acta Metallur. Sin. (English Lett.), vol. 29, no. 11, 2016, 10.1007/s40195-016-0472-4.
[29] G. Su and X. Gao, 'Comparison of medium manganese steel and Q345 steel on corrosion behavior in a 3.5 wt % NaCl solution', Materials, vol. 10, no. 8, 2017, 10.3390/ma10080938.
[30] A. HIGGINSON, R. C. NEWMAN, and R. P. M. PROCTER, 'ChemInform Abstract: The Passivation of Fe-Cr-Ru Alloys in Acidic Solutions', ChemInform, vol. 21, no. 7, 1990, 10.1002/chin.199007028.
[31] J. Guo, M. Seo, Y. Sato, G. Hultquist, C. Leygraf, and N. Sato, 'Electrochemical behavior and surface composition of copper containing ferritic stainless steel in sulfuric acid solution.', Boshoku gijutsu, vol. 35, no. 5, 1986, 10.3323/jcorr1974.35.5_283.
[32] M. Reffass, R. Sabot, C. Savall, M. Jeannin, J. Creus, and P. Refait, 'Localised corrosion of carbon steel in NaHCO3/NaCl electrolytes: Role of Fe(II)-containing compounds', Corros. Sci. vol. 48, no. 3, 2006, 10.1016/j.corsci.2005.02.016.
[33] R. E. Melchers, 'Effect of small compositional changes on marine immersion corrosion of low alloy steels', Corros Sci, vol. 46, no. 7, 2004, 10.1016/j.corsci.2003.10.004.
[34] 'Specialty Steel Industry of North Ammerican: galvanic corrosion', https://www.ssina.com/education/corrosion/galvanic-corrosion/ . Accessed: Jul. 24, 2024. [Online]. Available: https://www.ssina.com/education/corrosion/galvanic-corrosion/.
[35] B. Chico, D. De la Fuente, I. Díaz, J. Simancas, and M. Morcillo, 'Annual Atmospheric Corrosion of Carbon Steel Worldwide. An Integration of ISOCORRAG, ICP/UNECE and MICAT Databases', Materials, vol. 10, no. 6, 2017, 10.3390/ma10060601.
[36] S.K. Coburn, C.P. Larrabee, H.H. Lawson, O.B. Ellis, Corrosiveness of various atmospheric test sites as measured by specimens of steel and zinc, ASTM Spec. Tech. Publ. (1968), https://doi.org/10.1520/STP34098S.
[37] D. D. N. Singh, S. Yadav, and J. K. Saha, 'Role of climatic conditions on corrosion characteristics of structural steels', Corros. Sci. vol. 50, no. 1, 2008, 10.1016/j.corsci.2007.06.026.
[38] J. F. Marco, M. Gracia, J. R. Gancedo, M. A. Martín-Luengo, and G. Joseph, 'Characterization of the corrosion products formed on carbon steel after exposure to the open atmosphere in the Antarctic and Easter Island', Corros. Sci. vol. 42, no. 4, 2000, 10.1016/S0010-938X(99)00090-6.
[39] W. Thandar, Y.Y.K. Win, T. Khaing, Y. Suzuki, K. Sugiura, I. Nishizaki, Investigation of initial atmospheric corrosion of carbon and weathering steels exposed to urban atmospheres in Myanmar, Int. J. Corros. 2022 (2022), https://doi.org/10.1155/2022/4301767.
[40] Y. Seechurn, B. Y. R. Surnam, and J. A. Wharton, 'Marine atmospheric corrosion of carbon steel in the tropical microclimate of Port Louis', Mater. Corros. vol. 73, no. 9, 2022, 10.1002/maco.202112871.
[41] J. Huang et al., 'Atmospheric corrosion of carbon steels in tropical and subtropical climates in Southern China', Mater. Corros. vol. 71, no. 8, 2020, 10.1002/maco.201911487.
[42] T. T. J. Prošek, 'Exposure site catalogue: catalogue of atmospheric corrosion field exposure sites in europe.', 2021.
[43] N. S. Palsson, K. Wongpinkaew, P. Khamsuk, S. Sorachot, and W. Pongsaksawad, 'Outdoor atmospheric corrosion of carbon steel and weathering steel exposed to the tropical-coastal climate of Thailand', Mater. Corros. vol. 71, no. 6, 2020, 10.1002/maco.201911340.
[44] Y. C. Sica, E. D. Kenny, K. F. Portella, and D. F. Campos Filho, 'Atmospheric corrosion performance of carbon steel, galvanized steel, aluminum and copper in the North Brazilian coast', J. Braz. Chem. Soc. vol. 18, no. 1, 2007, 10.1590/S0103-50532007000100017.